

## Supplementary Materials for

### **A common hub for sleep and motor control in the substantia nigra**

Danqian Liu, Weifu Li, Chenyan Ma, Weitong Zheng, Yuanyuan Yao, Chak Foon Tso, Peng Zhong, Xi Chen, Jun Ho Song, Woochul Choi, Se-Bum Paik, Hua Han, Yang Dan\*

\*Corresponding author. E-mail: [ydan@berkeley.edu](mailto:ydan@berkeley.edu)

Published 24 January 2020, *Science* **367**, 440

DOI: [10.1126/science.aaz0956](https://doi.org/10.1126/science.aaz0956)

#### This PDF file includes:

Materials and Methods  
Figs. S1 to S9  
Table S1  
Captions for Movies S1 to S4  
References

#### Other Supplementary Material for this manuscript includes the following:

(available at [science.scienccemag.org/content/367/6476/440/suppl/DC1](https://science.scienccemag.org/content/367/6476/440/suppl/DC1))

Movies S1 to S4

## Materials and Methods

### Animals

All procedures were approved by the Animal Care and Use Committees of the University of California, Berkeley. Optogenetic manipulation experiments were performed in male and female *Gad2*<sup>Cre</sup> (Jackson Laboratory stock 010802), *Pvalb*<sup>Cre</sup> (008069), *TH*<sup>Cre</sup> (European Mouse Mutant Archive, EM00254) and *Nts*<sup>Cre</sup> (017525) mice. Mice were housed in 12-hour (h) light-dark cycle (lights on at 07:00 am and off at 07:00 pm) with free access to food and water. Animals with implants were housed individually.

### Virus preparation

AAV2-EF1 $\alpha$ -DIO-ChR2-eYFP, AAV2-EF1 $\alpha$ -DIO-iC++-eYFP, AAV2-EF1 $\alpha$ -DIO-eYFP, AAV2-EF1 $\alpha$ -DIO-hM3D(q)-mCherry, AAV2-EF1 $\alpha$ -DIO-hM4D(i)-mCherry, AAV2-EF1 $\alpha$ -DIO-mCherry were obtained from the University of North Carolina (UNC) vector core. AAV2-CAG-FLEX-TCB (TVA-mCherry), AAV2-CAG-FLEX-TC66T, AAV2-EF1 $\alpha$ -FLEX-eGFP-2a-TVA, AAV2-CAG-FLEX-RG (RG, rabies glycoprotein; vector constructs were gifts from L. Luo) were prepared in house according to previously described protocols (31). RG-deleted, eGFP-expressing rabies virus (RV- $\Delta$ G-eGFP) was purchased from Gene Transfer Targeting and Therapeutics Core of Salk Institute, RV- $\Delta$ G-tdTomato was a gift from B. Lim. RV was amplified in B7GG cells, pseudotyped with BHK-EnvA cells, and titered with HEK293-TVA cells (32).

### Surgical procedures

Adult mice (6-12 weeks old) were anesthetized with 1.5-2% isoflurane and placed on a stereotaxic frame. Body temperature was kept stable throughout the procedure using a heating pad. After asepsis, the skin was incised to expose the skull, and the overlying connective tissue was removed. To implant electroencephalogram (EEG) and electromyogram (EMG) recording electrodes, one stainless steel screw was inserted into the skull 1.5 mm from midline and 1.5 mm anterior to the bregma, and one inserted 2.5 mm from midline and 3 mm posterior to the bregma. Two EMG electrodes were inserted into the neck musculature. A reference screw was inserted into the skull on top of the right cerebellum. Insulated leads from the EEG and EMG electrodes were soldered to a pin header, which was secured to the skull using dental cement.

For optogenetic activation/inactivation experiments, a craniotomy (0.5-1 mm diameter) was made, and 0.1-0.2  $\mu$ l virus was injected into the target region (see below for coordinates) using Nanoject II (Drummond Scientific) via a micro pipette. Optic fibers (0.2 mm diameter; Thorlabs) were implanted into the target region with the tip 0.2 mm above the virus injection site two weeks after viral injection. Dental cement was applied to cover the exposed skull completely and to secure the implants for EEG and EMG recordings to the screws. For chemogenetic experiments, ~0.2  $\mu$ l AAV2-EF1 $\alpha$ -DIO-hM3D(q)-mCherry, AAV2-EF1 $\alpha$ -DIO-hM4D(i)-mCherry, or AAV2-EF1 $\alpha$ -DIO-mCherry was injected into SNr, implants for EEG and EMG recordings were implanted 2-3 weeks later. For optrode recording experiments, a custom-made optrode assembly was implanted into the SNr. The optrode assembly was secured to the skull together with EEG and EMG electrodes using dental cement. For local chemogenetic activation of axon terminals, a bilateral guide cannula (Plastics One) was inserted into the target region. After surgery, mice were allowed to recover for at least one week before experiments.

For rabies-mediated retrograde transsynaptic tracing from SNr neurons, ~0.3 µl of mixed AAV2-CAG-FLEX-TCB and AAV2-CAG-FLEX-RG was injected into the SNr of the corresponding Cre mice. For rabies tracing from the VTA, AAV2-CAG-FLEX-TC<sup>66T</sup> was used instead of AAV-TCB to avoid local contamination (33). Three weeks later, RV-ΔG-eGFP was injected into the same region, and mice were sacrificed 5-6 days later for histology. For rabies-mediated tracing of collateral projections, ~0.2 µl AAV2-CAG-FLEX-TVA-eGFP was injected into the SNr of *Gad2*<sup>Cre</sup> mice. After two weeks, ~0.2 µl RV-ΔG-tdTomato was injected into the thalamus or DR, and mice were sacrificed 3 days later. Collateral axonal signals were enhanced by immunostaining.

Stereotaxic coordinates for injections/implantations:

SNr: anteroposterior (AP) -3.0 mm, mediolateral (ML) 1.4 mm, dorsoventral (DV) 4.6 mm.

VM (thalamus): AP -1.5 mm, ML 0.9 mm, DV 4.2 mm.

DR: AP -4.3 mm, ML 0 mm, DV 3.2 mm.

VTA: AP -2.8 mm, ML 0.3 mm, DV 4.5 mm.

MLR: AP -4.2 mm, ML 0.9 mm, DV 3.5 mm.

LC: AP -5.0 mm, ML 1.1 mm, DV 3.7mm.

SCm: AP -3.4 mm, ML 1.6 mm, DV 1.8mm. STN: AP -2.0 mm, ML 1.7 mm, DV 4.6 mm.

### Behavioral recording and analysis

Behavioral experiments were carried out in home cages placed in sound-attenuating boxes between 9:00 am and 7:00 pm. Mouse behavior was recorded using a video camera at 30 frames per second (fps), along with EEG and EMG recordings. EEG and EMG electrodes were connected to flexible recording cables via a mini-connector. Recordings started after 20-30 min of habituation. The signals were recorded with a TDT RZ5 amplifier, filtered (0–300 Hz) and digitized at 1,500 Hz. Spectral analysis was carried out using fast Fourier transform (FFT), and brain states were classified into wake (desynchronized EEG and high EMG activity) and sleep state (NREM: synchronized EEG with high delta power (1-4 Hz) and low EMG activity; REM: high EEG theta power (6-9 Hz) and low EMG activity. The classification was made using a custom-written graphical user interface (programmed in MATLAB, MathWorks).

Automated tracking of the mouse motor behavior was performed using U-Net (34), a convolutional neural network for semantic segmentation at high accuracy and efficiency. The video recordings were down-sampled to 6 fps. We trained the U-Net model using ~3000 video frames with manual labelling (binary images showing the mouse body). The frames for training were randomly chosen ( $n = 4$  mice from two different recording setups) and covered as many conditions as possible (varied mouse postures, luminance conditions, etc.). Labeled data was randomly split into training and validation dataset (80% and 20%, respectively). The network was trained by minimizing the binary cross-entropy loss between the predicted score-map and the ground-truth (manual labelling) and then validated by the validation dataset. During the training process, we used a batch size of 1, performed data augmentation, and adopted the stochastic gradient descent (SGD) implementation of keras (an open-source neural-network library written in Python) with a fixed learning rate 0.005 and a momentum 0.9. Around 90,000 steps in total were enough for convergence in the presented cases, and training takes up to 42 h on a GPU (NVIDIA Tesla K40m) (35). The output from U-Net that is a predicted probability map will be binarized to get the segmentation result. The accuracy for the automated tracking was confirmed by calculating pixel

errors between the segmentation result with manual labelling in 500 video frames (fig. S1, B and C). The model accuracy is ~95% (relative to total body pixels), at a level similar to manual variability (difference between different sets of manual labelling, manual1 vs manual2), and much higher than an intensity-based image thresholding algorithm (~80%). To monitor the mouse's motor activity, two parameters were extracted by comparing segmented results across video frames: translation and total movement. Translation was measured by calculating changes in center of mass of the mouse body. Total movement was measured by calculating the total number of pixel differences of the segmented mouse body. The two parameters estimated based on the automated segmentation method was similar to those based on manual labelling (fig. S1D), but those based on the thresholding algorithm over-estimate both parameters.

To infer the natural structure of mouse's motor states, we first used Gaussian Mixture Model (an unsupervised clustering algorithm) for a clustering analysis (36). Motor activity of the mouse fell into three distinct clusters: high translation and high total movement, moderate translation and high total movement, and low translation and low total movement. Inspection of the video showed that these three clusters correspond to locomotion (LM), non-locomotor movements (MV) and immobility. To achieve behavioral classification at a higher accuracy, we then used a random forest model (a supervised classification algorithm). The training data for the random forest model were from four recording sessions, with translation and total movement as input parameters and motor state (manual labeling) as the output. The classification accuracy of the model assessed by a separate testing dataset was ~96%. The immobile state can be further divided into quiet wakefulness (QW) and sleep (SL) based on the brain state classification by polysomnographic recordings (described above). The classification of motor states and brain states is further cross-validated. For example, sleep epochs almost exclusively fall into the immobile motor state; LM and MV motor states are always within brain states classified as wakefulness.

Laser-induced effects on the state percentages or transition probabilities were measured by calculating the difference between the period during laser stimulation (120-s for activation and 60-s for inactivation) and that before laser stimulation (same duration as laser stimulation). To calculate the cumulative probability for sleep initiation (Fig. 3, D and I), only the trials with wakefulness >30 s before laser onset were included; for sleep termination, only the trials with sleep state at laser onset were included; for movement initiation, only the trials with immobile state (including QW and SL) at laser onset were included; for movement termination, only the trials with mobile state (including LM and MV) were included; for entering nest, only the trials with mice out of nest were included. The boundary of mouse's nest for each recording session was manually determined.

## Optogenetic manipulation

Optic fiber was attached through an FC/PC adaptor to a 473-nm blue laser diode (Shanghai laser), and light pulses were generated using the TDT system. For SNr neurons, constant light (~2 mW at fiber tip) lasting for 120 s (activation) or 60 s (inactivation) was used. For STN neurotensin-expressing neurons, high frequency laser (50 Hz, 10 ms per pulse, 1 mW, 120 s) was used; the lower laser power was used to avoid activating the neurotensin-expressing neurons in the nearby lateral hypothalamus. For all optogenetic manipulation experiment, inter-trial interval was set randomly from a uniform distribution between 7 and 15 min. Each experimental session lasted for 3-5 h (10-20 trials), and each animal was tested for 6-10 sessions.

## **Chemogenetic manipulation**

Saline (0.9% NaCl) or CNO (1 mg/kg, dissolved in saline) was injected intraperitoneally (i.p.) into mice expressing hM3Dq-mCherry, hM4Di-mCherry, or mCherry alone in the SNr. Each recording session started at 15 min after injection and lasted for 4 hours. Each mouse was recorded for 6-8 sessions, and CNO was given randomly in half of the sessions and saline in the other half. Data were averaged across all sessions for statistical comparison. For local chemogenetic activation of SNr GAD2 neuron axons, CNO (3  $\mu$ M, 500 nl) or saline was infused into the target region through the bilateral cannula, at 250 nl/min using a two-channel microinfusion pump. Each mouse was recorded for 2 sessions (randomly with CNO in the first, saline in the second; or saline in the first, CNO in the second session) with an interval of at least 2 days.

## **Optrode recording**

Custom-made optrodes (37) consisted of an optic fiber (200  $\mu$ m in diameter) glued together with 6 pairs of stereotrodes. Two FeNiCr wires (Stablohm 675, California Fine Wire) were twisted together and electroplated to an impedance of  $\sim$  200 k $\Omega$  using a custom-built plating device. The optrode was attached to a driver to allow vertical movement of the optrode assembly. Wires to record cortical EEG and EMG from neck musculatures were also attached for simultaneous recordings. A TDT RZ5 amplifier was used for all the recordings, signals were filtered (0.3-8 kHz) and digitized at 25 kHz. At the end of the experiment, an electrolytic lesion was made by passing a current (100  $\mu$ A, 10 s) through one or two electrodes to identify the end of the recording tract.

Spikes were sorted offline based on the waveform energy and the first three principal components of the spike waveform on each stereotrode channel. Single units were identified automatically using the software KlustaKwik (<http://klustakwik.sourceforge.net>). The quality of each unit was assessed by the presence of a refractory period and quantified using isolation distance and L-ratio. Units with an isolation distance  $<$  20 and L-ratio  $>$  0.1 were discarded.

To identify ChR2-tagged neurons, laser pulse trains (15 and/or 30 Hz with duration of 1 and 0.5 s, respectively) were delivered every 1 or 2 min. A unit was identified as ChR2 expressing if spikes were evoked by laser pulses reliably with short first-spike latency ( $<$  8 ms for all units in our sample), and with the waveforms of the laser-evoked and spontaneous spikes highly similar (correlation coefficient  $>$  0.98). To calculate the average firing rate of each unit in each brain state, spikes during the laser pulse trains were excluded.

To quantify the modulation of each neuron by motor activity, we computed correlation coefficient (CC) between its firing rate and EMG power during the entire recording session (2.5 s/bin). Neurons with CC  $>$  0 at P  $<$  0.05 (Pearson's correlation coefficient) were defined as movement-activated, neurons with CC  $<$  0 at P  $<$  0.05 as movement-suppressed, and neurons with P  $>$  0.05 as unmodulated. To compare the population activity for each subpopulation, the firing rate of each neuron was normalized by its mean during the whole recording session (with laser period excluded) and then averaged across neurons.

## **Immunohistochemistry and fluorescence *in situ* hybridization (FISH)**

Mice were deeply anaesthetized and transcardially perfused with 0.1M PBS followed by 4% paraformaldehyde (w/v) in PBS. For fixation, brains were kept overnight in 4% paraformaldehyde.

For cryoprotection, brains were placed in 30% sucrose (w/v) in PBS solution for 36-48 h. After embedding and freezing, brains were sectioned into 50- $\mu$ m coronal slices using a cryostat. For immunohistochemistry, brain slices were washed using PBS three times, permeabilized using PBST (0.3% Triton X-100 in PBS) for 30 min and then incubated with blocking solution (5% normal goat serum or normal donkey serum in PBST) for 1 hour followed by primary antibody incubation overnight at 4 °C using anti-GFP (GFP-1020, Aves Labs, 1:500), anti-PV (24428, Immunostar, 1:1,000), anti-TH (ab112, Abcam, 1:500), anti-calretinin (MAB1568, MilliporeSigma, 1:400) and anti-RFP (600-401-379, Rockland, 1:500) antibodies. The next day, slices were washed with PBS and incubated with appropriate secondary antibodies for 2 h (1:1000, All from Invitrogen): A-11039, Alexa Fluor 488 goat anti-chicken IgG and A-11012, Alexa Fluor 546 goat anti-rabbit IgG. FISH was done using RNAscope Multiplex Fluorescent v2 Assays according to the manufacturer's instructions (Advanced Cell Diagnostics). Cells with more than 10 fluorescent dots in the cytoplasm were considered as positively labeled. For whole-brain anterograde or retrograde tracing, one out of every four sections were imaged using 20 $\times$ , 0.75 NA objective in a high-throughput slide scanner (Nanoozoomer-2.0RS, Hamamatsu) for further processing. Other fluorescence images were taken using a fluorescence microscope (Keyence BZ-X710) or a confocal microscope (LSM 710 AxioObserver Inverted 34-Channel Confocal, Zeiss).

### **Quantification for output and input tracing**

Whole-brain mapping of SNr output projections was performed as previously described (38). Briefly, it contains three steps: (1) Registration: single coronal brain slices were aligned to the corresponding sections of the Allen Mouse Brain Atlas (© 2015 Allen Institute for Brain Science. Allen Brain Atlas API. Available from: [brain-map.org/api/index.html](http://brain-map.org/api/index.html)), by geometric transformations (translation, 2D rotation and scaling) based on several reference points. (2) Detection: fluorescence signals (eYFP) were detected using an intensity-based algorithm. For all slices from the same mouse, a single threshold was set; the threshold was optimized to preserve real fluorescence signals and eliminate noise pixels. The binarized result of each slice was compared with the original fluorescence image carefully, and the remaining noise pixels (normally caused by the uneven auto-fluorescence of the brain tissue) were rejected manually. (3) Quantification: the output (axon projection) to each region was quantified as the number of pixels occupied by detected axons, normalized by the total number of detected pixels in the entire brain (signals within ~1 mm radius of the injection site was excluded). Projections to nearby structures were thus likely to be underestimated. Confocal images were taken to determine local axonal projections.

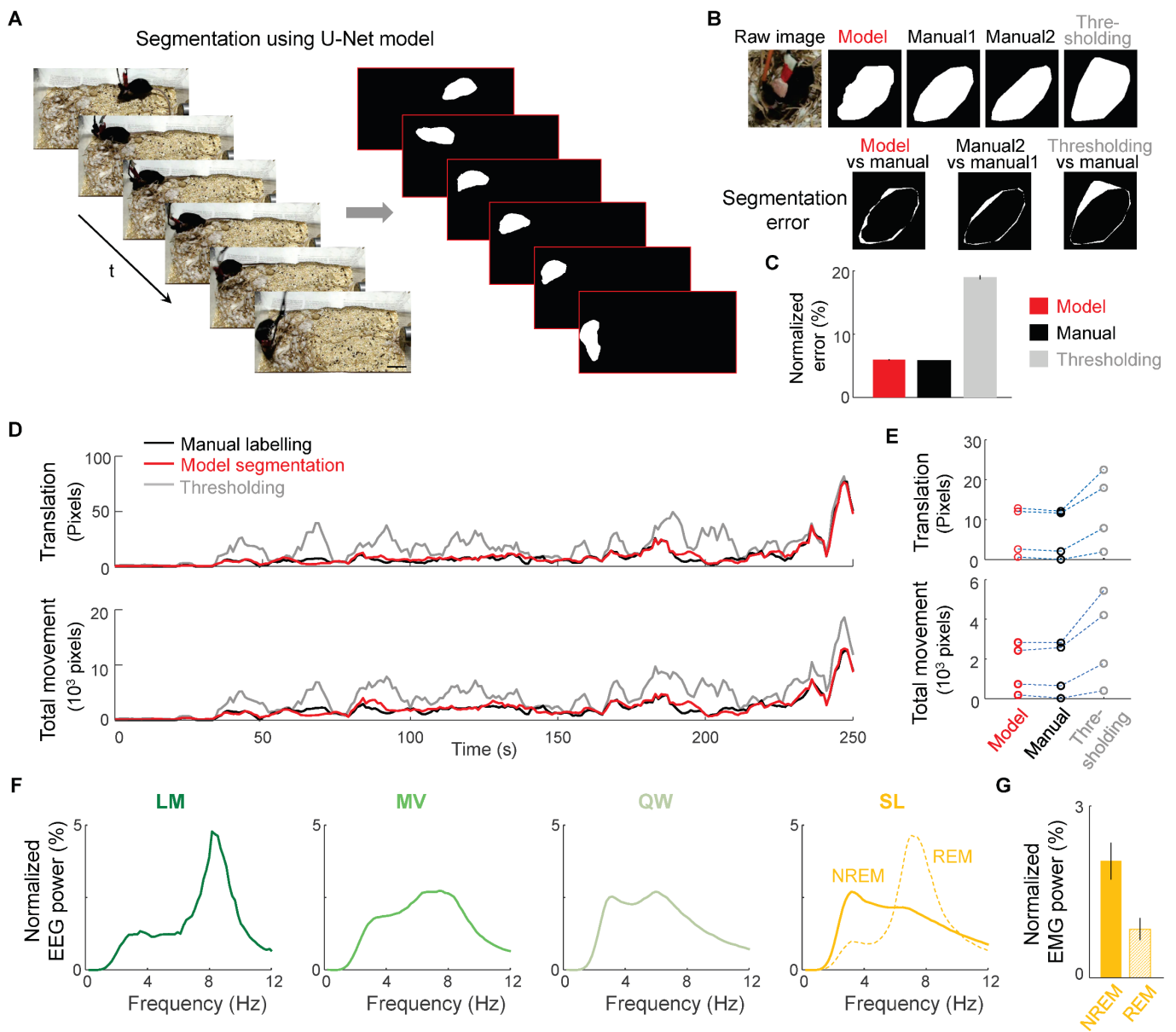
An automated method for calibrated single neuron mapping (AMaSiNe) (39) was adopted for quantification and 3-D reconstruction of input neurons. This method automatically calibrates the 3-D alignment angles of each brain slice to match the standardized 3-D Allen Mouse Brain Atlas and assign the position of each neuron in the atlas, which enables precise comparison of data from multiple brains on a common brain atlas. The number of detected neurons in each region was then divided by the total number of detected cells in the entire brain (after excluding the region within 1mm from the injection site).

Brain areas were grouped into 12 main structures according to the Allen Mouse Brain Atlas, but the basal ganglia (BG), including DS, NAc, GPe and GPi in the cerebral nucleus, STN,

pSTN in the hypothalamus was separately considered. PAG in the midbrain was grouped into MBsat instead of MBmot, given that the detected signals are mostly in the ventral PAG, which was more related to behavioral state. For brain structures containing >8% of outputs or >10% of inputs in either SNr populations, we further analyzed input/output distribution in specific brain areas; those with > 0.5% of total input/output are listed in Table S1. The mesencephalic locomotor region (MLR) includes the MRN, PPN and CUN.

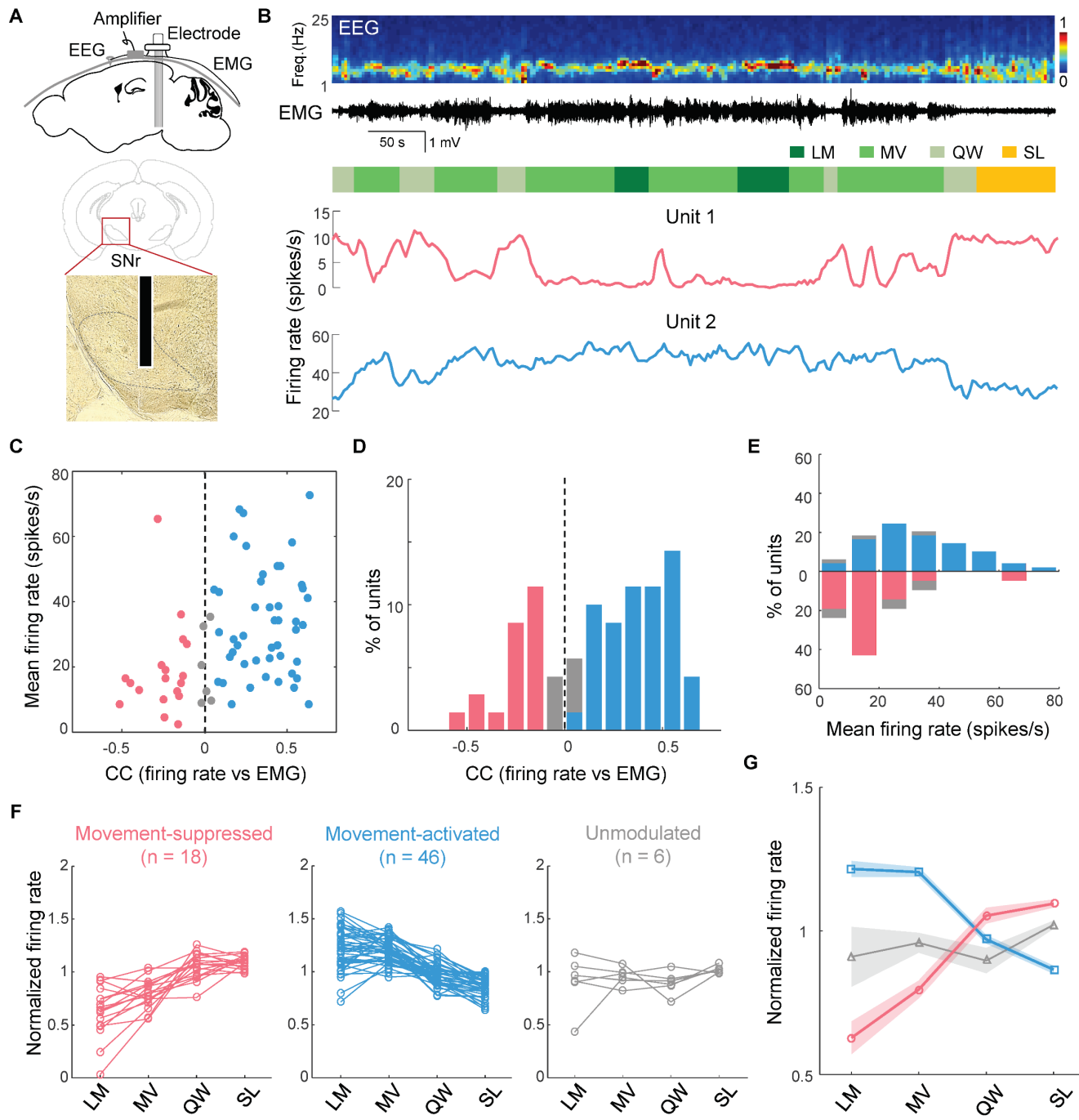
## Statistics

Statistical analysis was performed using Matlab. To analyze the effects of laser stimulation on behavioral states and transition probabilities in optogenetic experiments, the 95% confidence intervals (CIs) were calculated using a bootstrap procedure. For an experimental group of  $n$  mice, with mouse  $i$  comprising  $m_i$  trials, we repeatedly resampled the data by randomly drawing for each mouse  $m_i$  trials (random sampling with replacement). For each of the 10,000 iterations, we recalculated the mean across the  $n$  mice. The lower and upper confidence intervals were then extracted from the distribution of the resampled mean values. To test whether a given behavioral state or transition is significantly modulated by laser stimulation, we calculated for each bootstrap iteration the difference between the mean probabilities during laser stimulation and the preceding period of identical duration. Bootstrap was also used for testing the changes in normalized firing rate at state transitions. Two-way ANOVA with Bonferroni correction was used for comparisons of brain state between different conditions (saline or CNO) in chemogenetic experiments. To compare the degree of laser-induced (or CNO-induced) effects between groups of animals Mann–Whitney  $U$ -test was used. Two-sample Kolmogorov-Smirnov test was used to compare the cumulative probabilities in different groups.



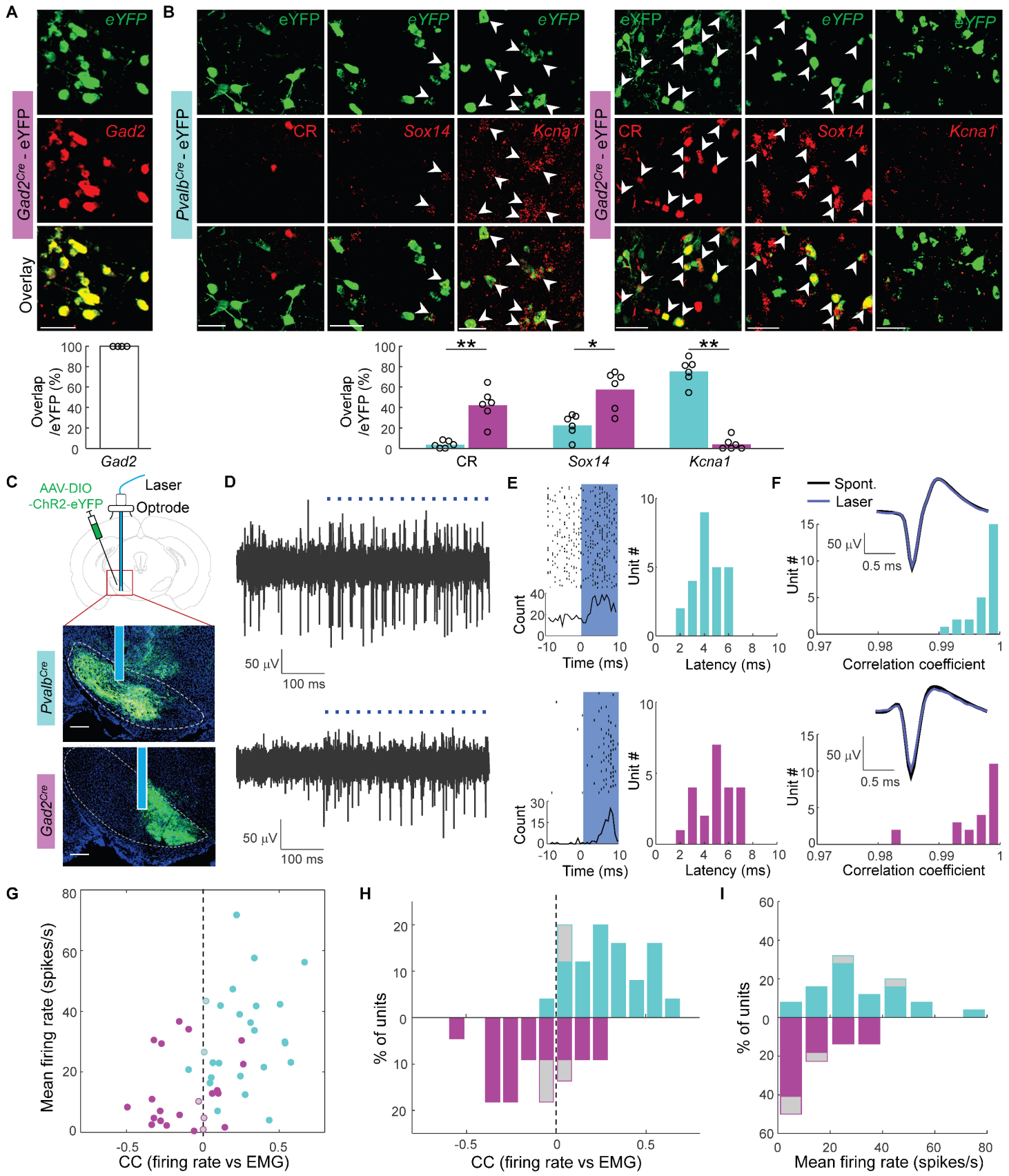
**Fig. S1. Automated tracking of freely moving mice in their home cage and EEG power spectra in different behavioral states.** (A) Example video frames and automated segmentation using a trained U-Net model. Shown are video frames at 1 s intervals. Scale bar: 100 pixels. (B) Errors of different segmentation methods for an example video frame. Top, the video image and segmentation results by the U-Net model, two trials of manual labeling, and intensity-based thresholding. Bottom, segmentation error, defined as the total number of pixels differing between segmentation results. (C) Quantification of segmentation error, calculated from 500 video frames. Segmentation error of each frame was normalized by the total number of pixels within the segmented white region. Segmentation error of the U-Net model is similar to the manual error. (D) Translation and total movement of a mouse based on manual, U-Net model, and thresholding-based segmentation in an example recording session. Note that the threshold-based segmentation causes over-estimation of both translation and total movement. (E) Average translation and total

movement based on different segmentation methods. Each line represents data from a randomly selected 200-s period. **(F)** Normalized EEG power spectra during different behavioral states, averaged from 9 mice. **(G)** Normalized EMG total power during NREM and REM sleep. For each mouse the EMG power was normalized by that of LM state (Fig. 1F) before averaged across mice. Error bar,  $\pm$ SEM.

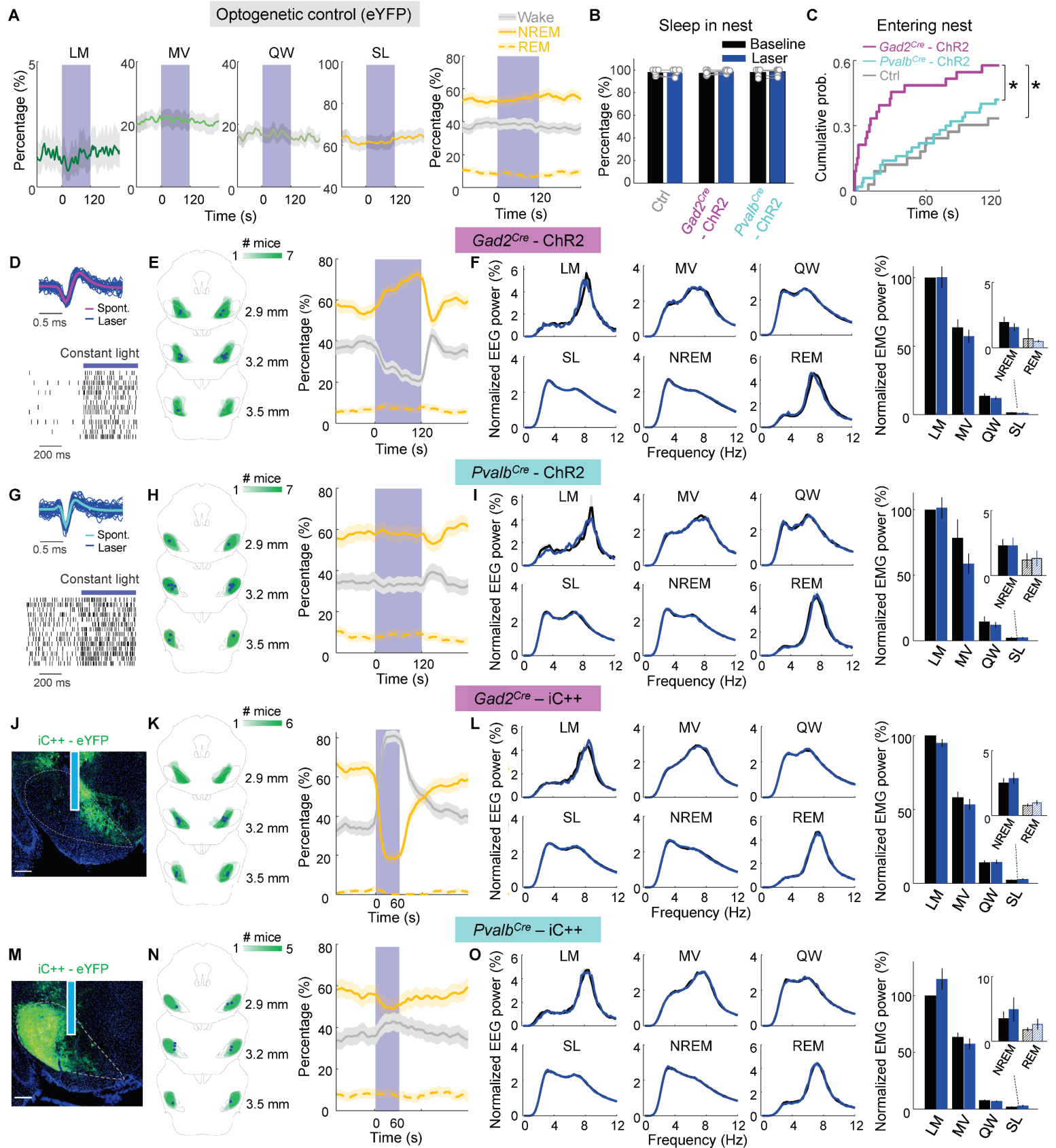


**Fig. S2. Firing rates of SNr neurons across different behavioral states.** **(A)** Schematic for extracellular recording from the SNr. **(B)** Firing rates of two simultaneously recorded SNr neurons in a single recording session, together with EEG spectrogram, EMG trace, and color-coded behavioral states. Freq., frequency. **(C)** Mean firing rate of each neuron was plotted against the correlation coefficient (CC) between its firing rate and EMG power. Each dot represents one neuron ( $n = 70$ ). **(D)** Distribution of CC (firing rate vs. EMG power) for all recorded neurons. Blue, neurons with  $CC > 0$  at  $P < 0.05$  (movement-activated); red, neurons with  $CC < 0$  (movement-suppressed). **(E)** Stacked histogram showing the percentage of units across mean firing rates for each behavioral state. **(F)** Three scatter plots showing normalized firing rate for Movement-suppressed ( $n = 18$ ), Movement-activated ( $n = 46$ ), and Unmodulated ( $n = 6$ ) neurons across behavioral states LM, MV, QW, and SL. **(G)** Line graph of Normalized firing rate across behavioral states for Movement-suppressed (red line), Movement-activated (blue line), and Unmodulated (grey line) neurons. Shaded regions indicate SEM.

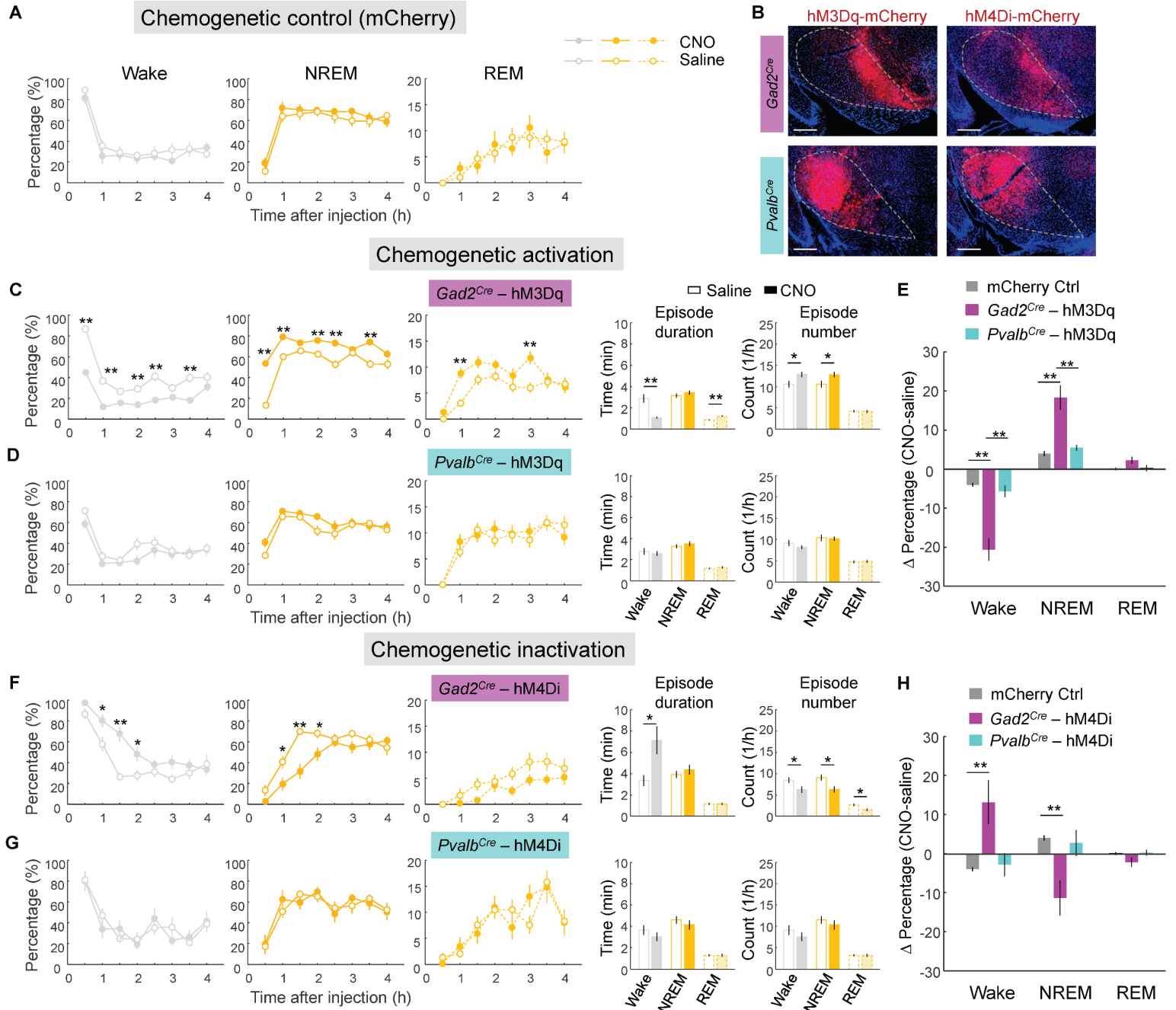
suppressed); Gray, CC not significantly different from 0 (unmodulated). **(E)** Distribution of mean firing rates of movement-activated, movement-suppressed, and unmodulated neurons. **(G)** Firing rates of the three types of neurons during different behavioral states. Firing rate of each neuron was normalized by its mean during the whole recording session. Each line indicates one neuron. **(H)** Mean firing rate of each type across different behavioral states. Shading,  $\pm$ SEM.



**Fig. S3. Optogenetic identification of SNr PV and GAD2 neurons.** **(A)** Dual FISH of *eYFP* and *Gad2* in the SNr showing all eYFP-labeled GAD2 neurons (labeled by Cre-inducible AAV injected into *Gad2*<sup>Cre</sup> mice) express *Gad2*. **(B)** Top, example images showing the overlap between eYFP and calretinin (CR, immunostaining), *Sox14* and *Kcnal1* (FISH) in the SNr of a *Pvalb*<sup>Cre</sup> (left) or *Gad2*<sup>Cre</sup> mouse (right). Arrows point to co-labeled cells. Scale bars, 50  $\mu$ m. Bottom, percentages of eYFP-labeled PV and GAD2 SNr neurons that express each marker ( $n = 6$  brain slices from at least 2 mice for each experiment). \* $P < 0.05$ , \*\* $P < 0.005$ , Mann–Whitney *U*-test. **(C)** Schematic for optrode recording and fluorescence images of SNr (red box in coronal diagram) in a *Pvalb*<sup>Cre</sup> and a *Gad2*<sup>Cre</sup> mouse injected with AAV-EF1 $\alpha$ -DIO-ChR2-eYFP. Scale bars: 200  $\mu$ m. **(D)** Raw traces of laser-evoked spikes from an identified PV (top) or GAD2 (bottom) neuron. Blue ticks, laser pulses. **(E)** Left, raster plot and peri-stimulus time histogram (PSTH) for laser-evoked spikes of example PV (top) and GAD2 (bottom) neurons. Right, distribution of latency of laser-evoked spiking for the 25 PV neurons (top) and 22 GAD2 neurons (bottom). The latency was measured by the mean delay time of the first spikes after laser onset. **(F)** Distribution of Pearson correlation coefficients between laser-evoked and spontaneous spike waveforms for all identified PV and GAD2 neurons. **(G)** Scatter plots for mean firing rate vs. correlation coefficient (CC) between firing rate and EMG power for all identified PV (cyan) and GAD2 (magenta) neurons. Each dot represents one neuron. **(H)** Distribution of CC (firing rate vs. EMG power) for PV (cyan) and GAD2 (magenta) neurons. **(I)** Distribution of mean firing rates of PV (cyan) and GAD2 (magenta) neurons.

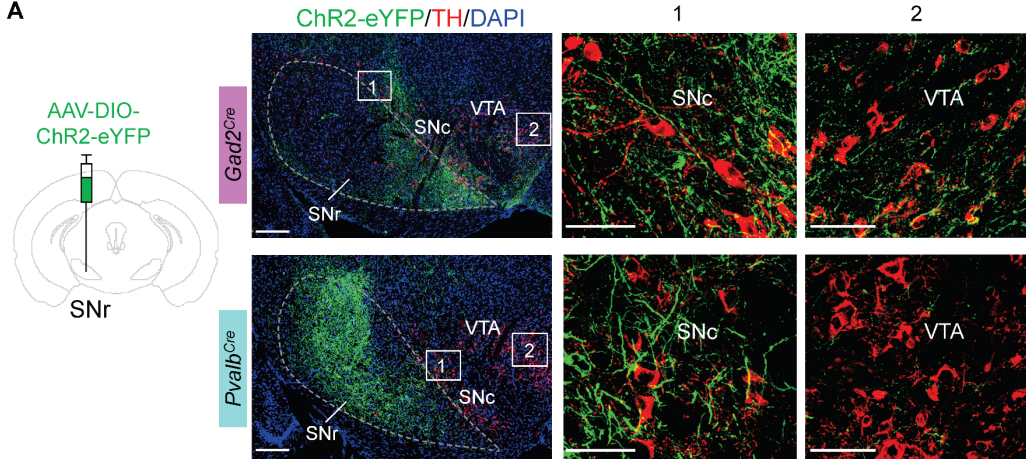
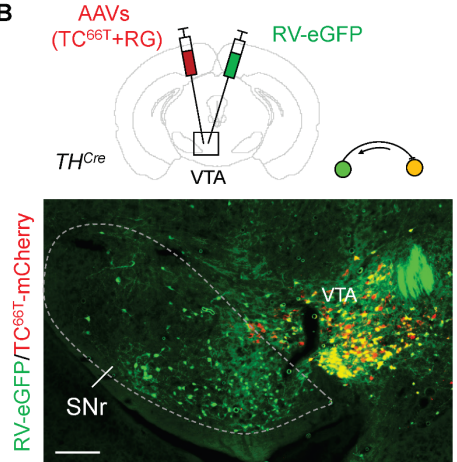
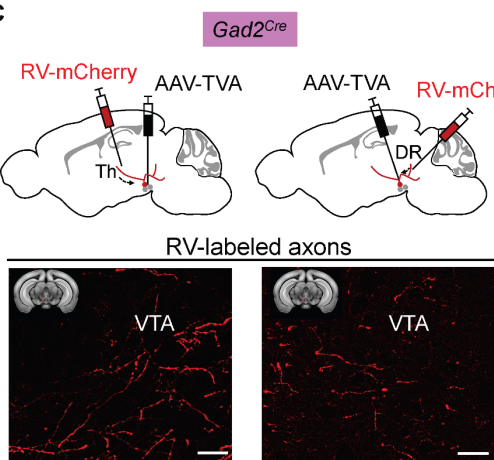
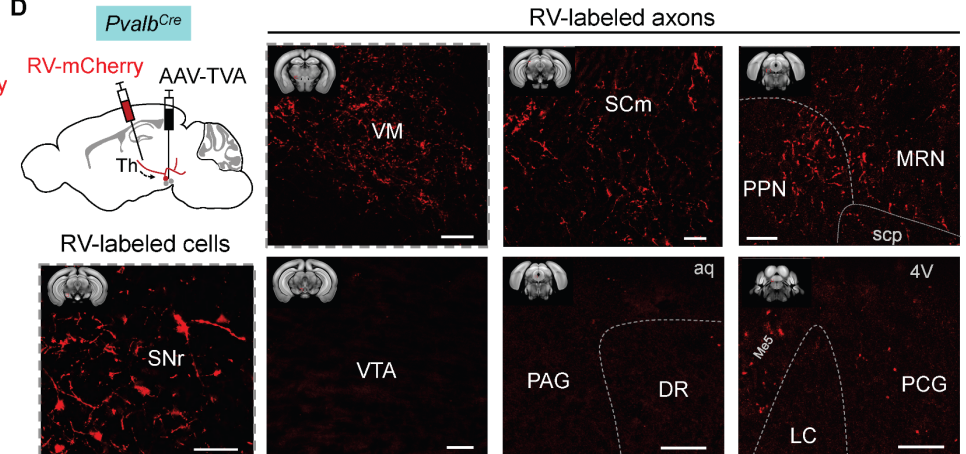


**Fig. S4. Optogenetic manipulation of SNr neurons does not alter EEG and EMG activity within each behavioral state.** **(A)** Effect of laser stimulation in control mice expressing eYFP only in the SNr. Shown are percentages of the four behavioral states (LM, MV, QW and SL, left) and three brain states (wake, NREM and REM, right) before, during and after laser stimulation (120 s), averaged from 6 mice. Shading, 95% CI. Blue stripe, laser stimulation period. P>0.2 for all states, bootstrap. **(B)** Percentages of sleep episodes in the nest during laser and baseline periods. Each pair of symbols connected by a line represents one mouse. P>0.05 for paired comparisons in control, *Gad2*<sup>Cre</sup>-ChR2 and *Pvalb*<sup>Cre</sup>-ChR2 mice, Wilcoxon signed rank test. **(C)** Cumulative probability of the mouse entering the nest during 120-s laser stimulation in control, *Gad2*<sup>Cre</sup>-ChR2 and *Pvalb*<sup>Cre</sup>-ChR2 mice. \*P<10<sup>-7</sup>, Kolmogorov-Smirnov test. **(D)** Top, spontaneous and laser-evoked spike waveform from an example identified GAD2 neuron. Bottom, spike raster showing firing rate increase induced by constant light. **(E)** Left, summary of ChR2-eYFP expression in *Gad2*<sup>Cre</sup> mice (n = 7). For each mouse, the spread of ChR2-eYFP in 3 brain sections (from -2.9 mm to -3.5 mm along the rostrocaudal axis, where most of the virus expression was observed) was determined. The green color code indicates in how many mice the virus was expressed at the corresponding location. Blue dots indicate the locations of optic fiber tips. Right, effect of laser stimulation on wakefulness, REM and NREM sleep. **(F)** Comparison of normalized EEG power spectra (left) and EMG total power (right) within each state in the 120-s period before (black) and during (blue) laser stimulation, averaged across 7 mice. For SL, NREM and REM states were also shown separately. Note that the EEG and EMG patterns are very similar between laser and baseline periods within each behavioral state. **(G)** An example recording from ChR2-tagged PV neuron showing firing rate increase induced by constant laser. **(H and I), (K and L), and (N and O)**, Similar to (E and F), but for *Pvalb*<sup>Cre</sup> – ChR2 (H and I), *Gad2*<sup>Cre</sup> – iC++ (K and L) and *Pvalb*<sup>Cre</sup> – iC++ (N and O) mice. **(J and M)** Fluorescence images of SNr in a *Gad2*<sup>Cre</sup> (J) and a *Pvalb*<sup>Cre</sup> (M) mouse injected with AAV-EF1α-DIO-iC++-eYFP. Scale bars, 200 μm.



**Fig. S5. Chemogenetic manipulation of SNr GAD2 but not PV neurons affects sleep.** (A) Control experiment showing the effect of CNO in *Gad2<sup>Cre</sup>* mice expressing mCherry only. Shown is the percentage of time in each brain state following CNO or vehicle injection. Horizontal axis, time after CNO/vehicle injection. Error bar,  $\pm$ SEM; n = 6 mice. There was no significant difference between CNO and vehicle injections (two-way ANOVA, condition (CNO vs. saline)  $\times$  time, P > 0.1 for the main effect of condition for wake, NREM and REM sleep). (B) Fluorescence images of SNr in *Gad2<sup>Cre</sup>* and *Pvalb<sup>Cre</sup>* mouse injected with AAV2-EF1 $\alpha$ -DIO-hM3D(q)-mCherry, and AAV2-EF1 $\alpha$ -DIO-hM4D(i)-mCherry. Scale bars, 200  $\mu$ m. (C) Chemogenetic activation experiment in *Gad2<sup>Cre</sup>* mice expressing hM3Dq in the SNr (n = 6 mice). Left, percentage of time

in each brain state following CNO or vehicle injection. \*P<0.05; \*\* P<0.001 (two-way ANOVA with Bonferroni correction). Right, mean duration and number of episodes for each state during 4-h recording. \*P<0.05; \*\*P<0.01, Mann–Whitney *U*-test. **(D)** Similar to (C), for chemogenetic activation in *Pvalb*<sup>Cre</sup> mice (n=6). **(E)** Left, changes in each state induced by chemogenetic activation (difference between CNO and saline injections, averaged across the 4-h after injection) in *Gad2*<sup>Cre</sup>, *Pvalb*<sup>Cre</sup> or mCherry control mice. Error bars represent SEM. \*P<0.05; \*\*P<0.01, Mann–Whitney *U*-test. **(F-H)** Similar to (C-E), but for chemogenetic inactivation experiment. *Gad2*<sup>Cre</sup> – hM4Di, n=6; *Pvalb*<sup>Cre</sup> – hM4Di, n = 4.

**A****B****C****Collateral tracing**

**Fig. S6. Innervation of the ventral tegmental area by SNr neurons.** (A) Confocal images with low (left) and high (middle and right) magnification showing axonal projections of SNr GAD2 and PV neurons in the substantia nigra pars compacta (SNC) and ventral tegmental area (VTA). Red fluorescence, tyrosine hydroxylase (TH) immunostaining. Scale bars, 200 µm (left) and 50 µm (middle and right). (B) Top, schematic showing viral injections for local retrograde tracing from VTA dopaminergic neurons. Bottom, fluorescence images showing starter cells (yellow) in the VTA and presynaptic cells (green) in the medial SNr. Scale bar, 200 µm. (C) Fluorescence images showing axonal collaterals of VM- or DR-projecting SNr GAD2 neurons in the VTA. (D) Fluorescence images showing RV-labeled VM-projecting PV neurons and their axonal collaterals in the SCm and MLR. Scale bars, 100 µm in (C) and (D).

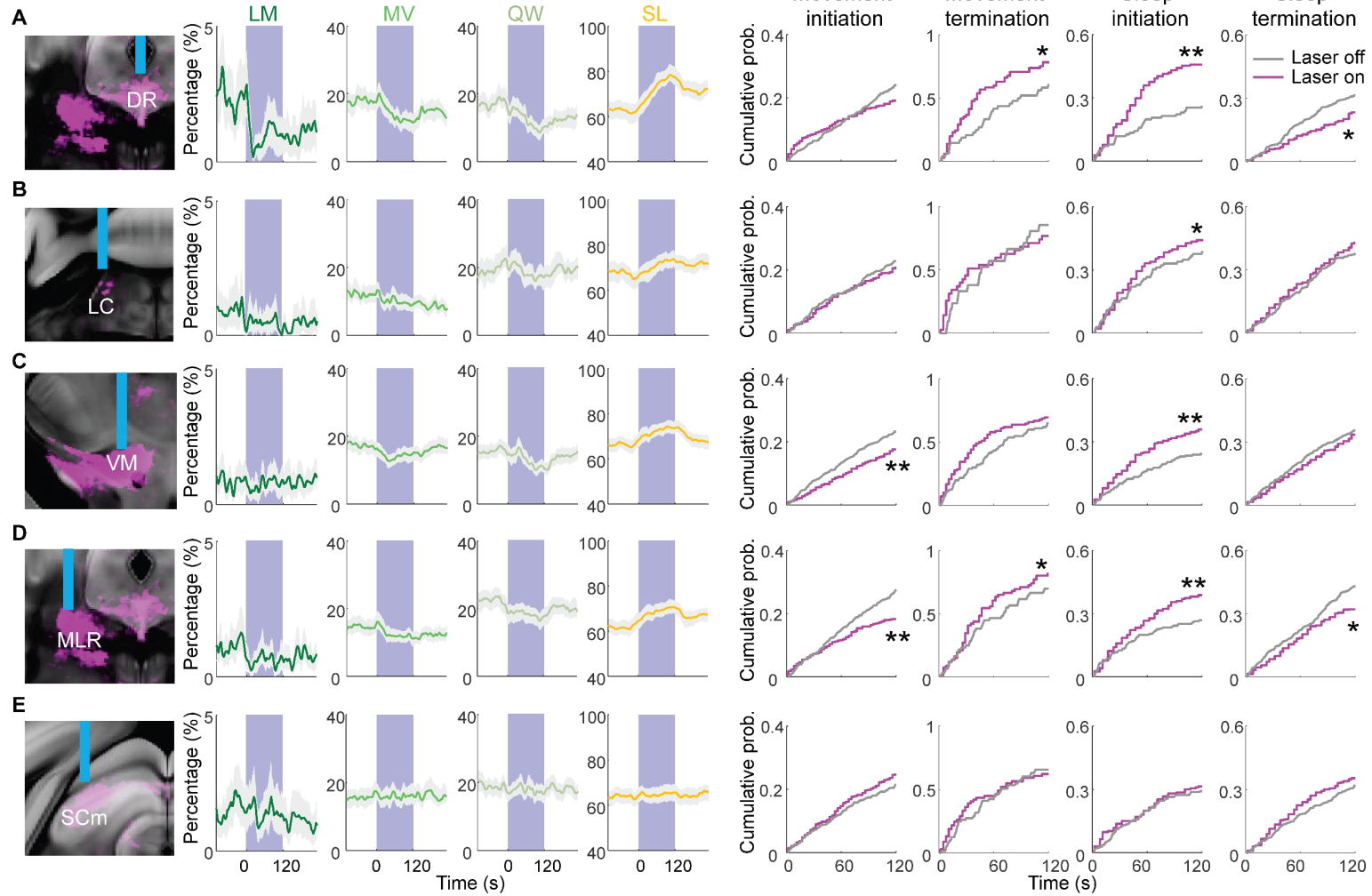
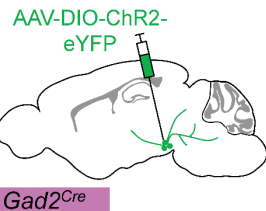


**Fig.S7. Effects of activating SNr GAD2 neuron terminals in different brain regions.** (A) Left, percentage of time in LM, MV, QW or SL state before, during, and after laser activation of SNr axons in DR (n=5 mice). Shading, 95% confidence intervals. Blue stripe, laser period (constant light, 120 s). Right, cumulative probabilities for movement initiation/termination and sleep initiation/termination during 120-s laser stimulation. \*P<10<sup>-4</sup>, \*\*P<10<sup>-7</sup> for comparison between laser on and laser off periods, Kolmogorov-Smirnov test. (B-E) Similar to (A), for terminal stimulation in LC (n=6), VM (n=7), MLR (n=5) and SCm (n=6). (F) Chemogenetic activation of SNr GAD2 neuron terminals in MLR and DR. Shown is the percentage of time in each brain state following CNO or vehicle injection. Horizontal axis, time after CNO/vehicle injection. Error bar, ±SEM; n=6 mice each. \*P < 0.05; \*\* P < 0.01, two-way ANOVA with Bonferroni correction.

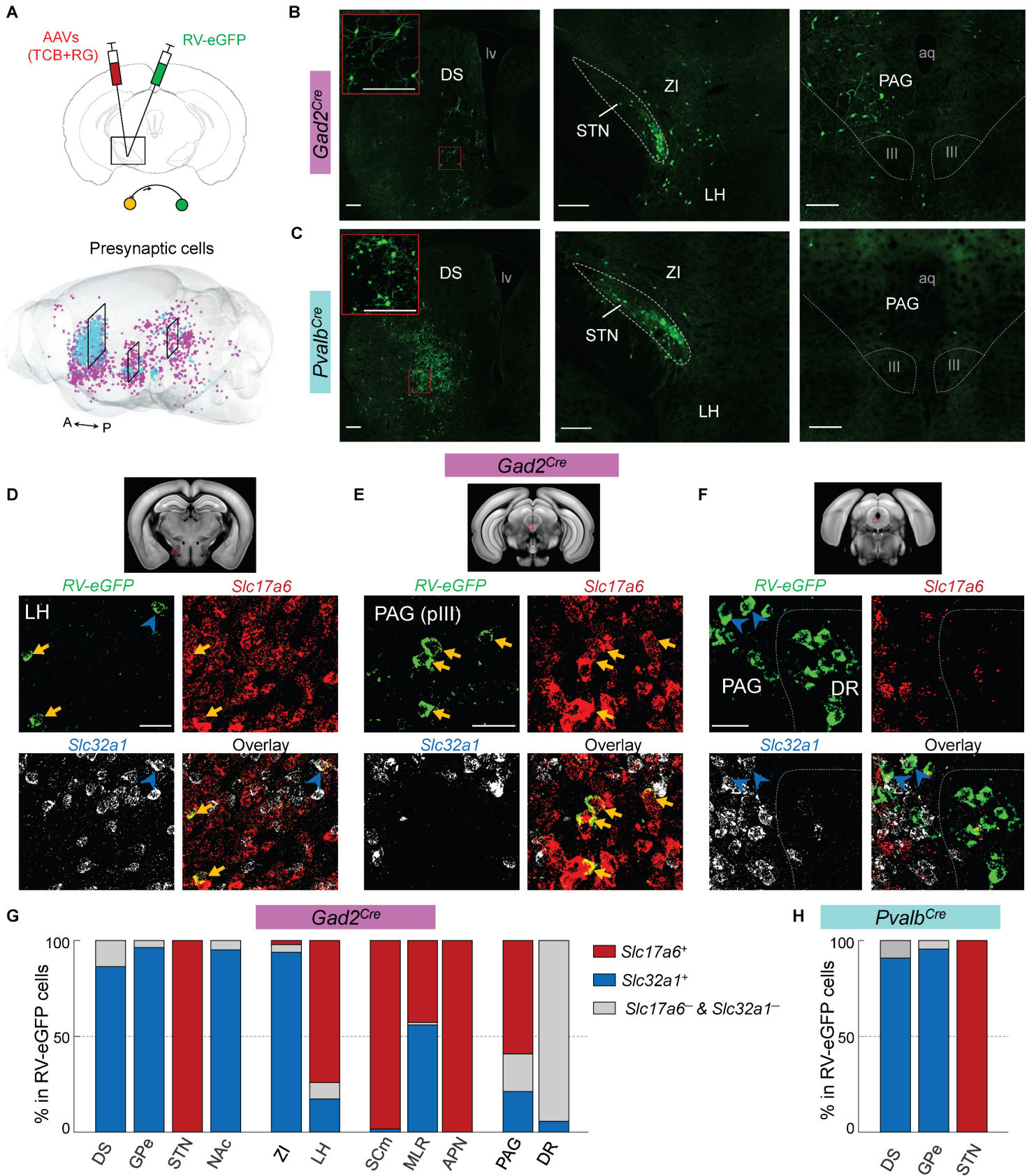


**Fig. S8. Monosynaptic input neurons to SNr GAD2 and PV neurons.** (A) Schematic for RV-mediated retrograde tracing and 3D reconstruction of inputs to SNr GAD2 (magenta) and PV (cyan) neurons, from one *Gad2*<sup>Cre</sup> and one *Pvalb*<sup>Cre</sup> mouse, respectively. (B) Fluorescence images showing input neurons to SNr GAD2 neurons in three brain regions, corresponding to black boxes from anterior to posterior in (A). Inset in the left panel shows higher magnification of the region in red box. Scale bars: 200 µm. DS, dorsal striatum; ZI, zona incerta; STN, subthalamic nucleus; LH, lateral hypothalamus; PAG, periaqueductal gray; lv, lateral ventricle; aq, cerebral aqueduct; III, oculomotor nucleus. (C) Similar to (B), showing input neurons to SNr PV neurons. (D) Triple FISH of *RV-eGFP*, *Slc17a6*, and *Slc32a1* in the LH. Yellow arrow: overlap between *RV-eGFP* and *Slc17a6*. Blue arrowhead, overlap between *RV-eGFP* and *Slc32a1*. Scale bars, 50 µm. (E and F) Similar to (D), for PAG near periocular motor region (pIII) and DR. (G) Percentage of RV-labeled presynaptic inputs to SNr GAD2 neurons in each region that were labeled by *Slc17a6*, *Slc32a1* or neither. (H), Similar to (G), for presynaptic inputs to SNr PV neurons.

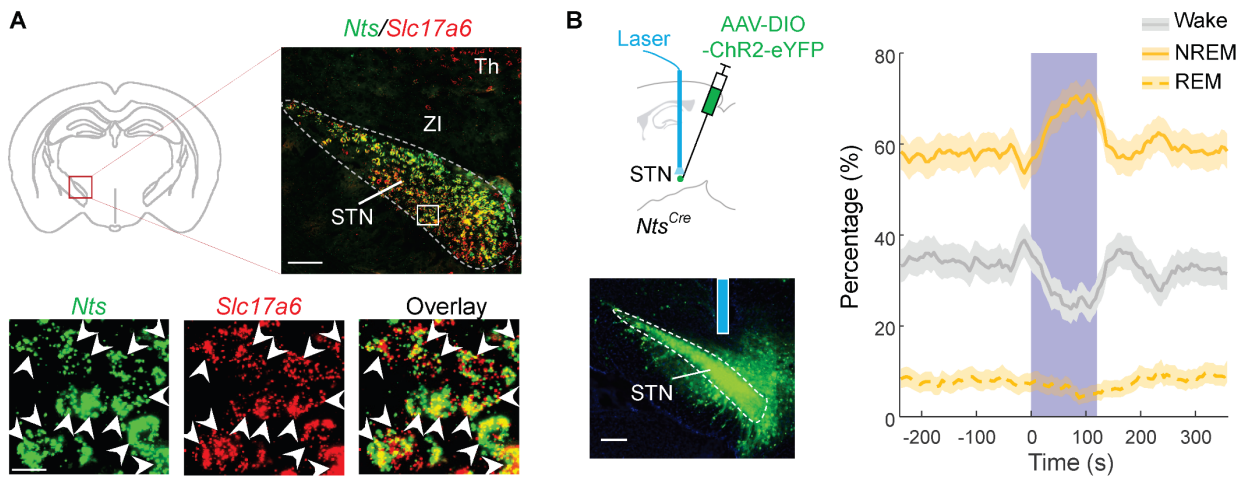


**Fig. S9. Activation of neurotensin-expressing glutamatergic neurons in the subthalamic nucleus promotes sleep. (A)** Top, overlap between neurotensin (*Nts*) and *Slc17a6* in the subthalamic nucleus (STN) based on double FISH. Red box in the coronal diagram indicates the region shown in the fluorescence image. Scale bar: 100  $\mu$ m. Bottom, high magnification fluorescence image of the region in the white box. Arrowheads indicate co-labeled neurons. Scale bar: 20  $\mu$ m. **(B)** Percentage of time in NREM, REM, or wake state before, during, and after optogenetic activation of neurotensin-expressing STN neurons ( $n = 6$  mice). Laser stimulation (50 Hz, 120 s) significantly increased NREM sleep ( $P < 0.0001$ , bootstrap) and decreased wakefulness ( $P < 0.0001$ ) and REM sleep ( $P = 0.02$ ). Shading, 95% CI. Scale bar, 100  $\mu$ m.

**Table S1. Summary for outputs and inputs of SNr neurons across brain regions.**

Brain structure	Abbreviation	Outputs (mean ± SEM %)		Inputs (mean ± SEM %)	
		GAD2	PV	GAD2	PV
<b>Cerebral cortex</b>	<b>Ctx</b>	0.00±0.00	0.00±0.00	3.37±1.10	0.91±0.56
<b>Cerebral nuclei</b>	<b>CNu</b>	1.71±0.72	0.18±0.09	7.04±0.79	1.79±0.52
<b>Basal ganglia</b>	<b>BG</b>	3.89±1.50	1.04±0.31	37.67±5.72	75.49±5.03
Dorsal striatum	DS	1.09±0.54	0.04±0.02	24.61±5.83	52.7±5.30
Nucleus accumbens	NAc	0.25±0.23	0.00±0.00	3.40±1.30	0.63±0.21
Globus pallidus, external segment	Gpe	0.04±0.03	0.15±0.07	4.82±1.13	14.39±4.01
Globus pallidus, internal segment	Gpi	0.38±0.17	0.18±0.09	0.22±0.11	0.22±0.13
Subthalamic nucleus	STN	0.87±0.22	0.61±0.16	3.33±0.73	6.78±1.64
Parasubthalamic nucleus	pSTN	1.27±0.57	0.16±0.01	1.29±0.49	0.77±0.28
<b>Thalamus</b>	<b>Th</b>	16.24±3.96	26.70±0.89	4.23±0.81	1.87±0.53
Ventral anterior-lateral complex	VAL	1.18±0.63	1.51±0.44	0.04±0.04	0.02±0.02
Ventral medial nucleus	VM	8.72±1.47	7.31±0.71	0.41±0.18	0.27±0.07
Ventral posterior complex	VP	0.37±0.19	1.37±0.17	0.36±0.12	0.40±0.17
Mediodorsal nucleus	MD	0.74±0.40	3.41±0.34	0.00±0.00	0.03±0.03
Parafascicular nucleus	PF	1.04±0.36	2.59±0.10	0.14±0.09	0.09±0.07
Other		4.20±1.44	10.48±0.64	3.29±0.74	1.05±0.52
<b>Hypothalamus</b>	<b>Hypoth</b>	14.14±3.07	5.57±0.13	10.33±1.13	8.24±0.77
Posterior hypothalamic nucleus	PH	0.81±0.70	0.04±0.03	0.38±0.12	0.04±0.02
Lateral hypothalamic area	LH	2.13±1.01	0.02±0.01	1.78±0.23	0.81±0.43
Zona incerta	ZI	7.65±0.48	4.82±0.22	4.66±0.79	4.03±0.91
Lateral preoptic area	LPO	0.92±0.67	0.00±0.00	0.18±0.06	0.03±0.02
Other		2.64±0.96	0.70±0.07	3.32±0.83	3.33±0.48
<b>Midbrain, sensory related</b>	<b>MBsen</b>	0.18±0.11	0.03±0.02	1.69±0.65	0.32±0.20
<b>Midbrain, motor related</b>	<b>MBmot</b>	36.50±3.96	61.25±1.72	18.59±3.04	7.27±2.21
Superior colliculus, motor related	SCm	7.56±2.43	25.74±0.56	8.18±1.82	3.07±0.98
Mesencephalic locomotor region	MLR	24.71±3.56	25.71±0.93	6.24±0.85	2.54±0.57
Midbrain reticular nucleus	MRN	16.7±2.48	22.64±1.37	4.58±0.70	1.67±0.41
Pedunculopontine nucleus	PPN	7.59±1.21	3.03±0.45	1.37±0.34	0.8±0.26
Cuneiform nucleus	CUN	0.42±0.19	0.04±0.02	0.29±0.06	0.07±0.06
Anterior pretectal area	APN	0.51±0.26	4.95±0.36	3.06±1.54	0.96±0.61
Red nucleus	RN	2.20±0.95	3.54±0.26	0.06±0.06	0.07±0.05
Other		1.95±0.22	1.35±0.29	1.34±0.06	0.70±0.21
<b>Midbrain, behavioral state related</b>	<b>MBsta</b>	8.40±1.37	1.84±0.47	10.28±1.14	1.63±0.30
Periaqueductal gray	PAG	5.69±0.85	1.78±0.47	8.75±1.12	1.28±0.21
Dorsal nucleus raphe	DR	1.49±0.20	0.04±0.03	1.27±0.42	0.30±0.10
Other		1.23±0.63	0.02±0.01	0.25±0.05	0.04±0.03
<b>Pons, sensory related</b>	<b>P-sen</b>	1.18±0.17	0.61±0.46	0.52±0.15	0.27±0.12
<b>Pons, motor related</b>	<b>P-mot</b>	0.86±0.14	0.83±0.72	1.48±0.16	0.22±0.13
<b>Pons, behavioral state related</b>	<b>P-sat</b>	16.32±2.32	0.94±0.41	1.43±0.20	0.53±0.25
Superior central nucleus raphe	CS	3.61±1.18	0.04±0.01	0.16±0.08	0.06±0.06
Pontine reticular nucleus	PRN	12.11±2.45	0.89±0.40	1.05±0.17	0.40±0.17
Dorsal lateral pons (peri-locus ceruleus area)	dLPons	0.60±0.29	0.00±0.00	0.16±0.06	0.07±0.06
Other		0.28±0.12	0.00±0.00	0.06±0.04	0.00±0.00
<b>Medulla</b>	<b>Medu</b>	0.57±0.44	0.99±0.92	1.99±0.47	0.49±0.40
<b>Cerebellum</b>	<b>Cereb</b>	0.00±0.00	0.00±0.00	1.39±0.26	0.97±0.85

### **Movie S1. Optogenetic activation of SNr GAD2 neurons suppresses movement and promotes sleep.**

Shown are EEG power spectrogram, EMG trace, motor activity (translation and total movement), color-coded behavioral states, and video recording of a *Gad2*<sup>Cre</sup> mouse expressing ChR2-eYFP in the SNr. Movement termination (trial 1), movement termination followed by sleep initiation (trials 2 and 3) and sleep maintenance (trail 4) were observed during laser stimulation (constant light, ~2 mW, 120 s). Laser stimulation period is depicted by the blue bar on the top and appearance of a blue circle at the upper left corner of the mouse video frame (bottom panel). Red outline shows automated segmentation of the mouse body. The video is shown at 5× the original speed. LM, locomotion; MV, non-locomotor movements; QW, quiet wakefulness; SL, sleep.

### **Movie S2. Optogenetic activation of SNr PV neurons suppresses movement**

Shown are EEG power spectrogram, EMG trace, motor activity (translation and total movement), color-coded behavioral states, and video recording of a *Pvalb*<sup>Cre</sup> mouse expressing ChR2-eYFP in the SNr. Laser stimulation period (constant light, ~2 mW, 120 s) is depicted by the blue bar on the top and appearance of a blue circle at the upper left corner of mouse video frame (bottom panel). Red outline shows automated segmentation of the mouse body. The video is shown at 5× the original speed. LM, locomotion; MV, non-locomotor movements; QW, quiet wakefulness; SL, sleep.

### **Movie S3. Whole-brain distributions of axons from SNr neurons.**

Shown are eYFP fluorescence signals for anterograde tracing from SNr GAD2 (magenta) and PV (cyan) neurons.

### **Movie S4. Whole-brain distributions of presynaptic inputs to SNr neurons.**

Shown are summary of presynaptic inputs to SNr GAD2 (magenta, n = 5 mice) and PV (cyan, n = 5) neurons. Gray circle represents region excluded from quantification (within 1 mm from the injection site).

## References and Notes

1. S. S. Campbell, I. Tobler, Animal sleep: A review of sleep duration across phylogeny. *Neurosci. Biobehav. Rev.* **8**, 269–300 (1984). [doi:10.1016/0149-7634\(84\)90054-X](https://doi.org/10.1016/0149-7634(84)90054-X) [Medline](#)
2. J. C. Hendricks, S. M. Finn, K. A. Panckeri, J. Chavkin, J. A. Williams, A. Sehgal, A. I. Pack, Rest in Drosophila is a sleep-like state. *Neuron* **25**, 129–138 (2000). [doi:10.1016/S0896-6273\(00\)80877-6](https://doi.org/10.1016/S0896-6273(00)80877-6) [Medline](#)
3. P. J. Shaw, C. Cirelli, R. J. Greenspan, G. Tononi, Correlates of sleep and waking in *Drosophila melanogaster*. *Science* **287**, 1834–1837 (2000). [doi:10.1126/science.287.5459.1834](https://doi.org/10.1126/science.287.5459.1834) [Medline](#)
4. D. Liu, Y. Dan, A motor theory of sleep-wake control: Arousal-action circuit. *Annu. Rev. Neurosci.* **42**, 27–46 (2019). [doi:10.1146/annurev-neuro-080317-061813](https://doi.org/10.1146/annurev-neuro-080317-061813) [Medline](#)
5. J. Peever, P. M. Fuller, The biology of REM sleep. *Curr. Biol.* **27**, R1237–R1248 (2017). [doi:10.1016/j.cub.2017.10.026](https://doi.org/10.1016/j.cub.2017.10.026) [Medline](#)
6. O. Hikosaka, R. H. Wurtz, Modification of saccadic eye movements by GABA-related substances. II. Effects of muscimol in monkey substantia nigra pars reticulata. *J. Neurophysiol.* **53**, 292–308 (1985). [doi:10.1152/jn.1985.53.1.292](https://doi.org/10.1152/jn.1985.53.1.292) [Medline](#)
7. A. V. Kravitz, B. S. Freeze, P. R. L. Parker, K. Kay, M. T. Thwin, K. Deisseroth, A. C. Kreitzer, Regulation of parkinsonian motor behaviours by optogenetic control of basal ganglia circuitry. *Nature* **466**, 622–626 (2010). [doi:10.1038/nature09159](https://doi.org/10.1038/nature09159) [Medline](#)
8. C. R. Gerfen, D. J. Surmeier, Modulation of striatal projection systems by dopamine. *Annu. Rev. Neurosci.* **34**, 441–466 (2011). [doi:10.1146/annurev-neuro-061010-113641](https://doi.org/10.1146/annurev-neuro-061010-113641) [Medline](#)
9. C. Ma, P. Zhong, D. Liu, Z. K. Barger, L. Zhou, W.-C. Chang, B. Kim, Y. Dan, Sleep regulation by neurotensinergic neurons in a thalamo-amygdala circuit. *Neuron* **103**, 323–334.e7 (2019). [doi:10.1016/j.neuron.2019.05.015](https://doi.org/10.1016/j.neuron.2019.05.015) [Medline](#)
10. X. Jin, F. Tecuapetla, R. M. Costa, Basal ganglia subcircuits distinctively encode the parsing and concatenation of action sequences. *Nat. Neurosci.* **17**, 423–430 (2014). [doi:10.1038/nn.3632](https://doi.org/10.1038/nn.3632) [Medline](#)
11. G. Rizzi, K. R. Tan, Synergistic nigral output pathways shape movement. *Cell Rep.* **27**, 2184–2198.e4 (2019). [doi:10.1016/j.celrep.2019.04.068](https://doi.org/10.1016/j.celrep.2019.04.068) [Medline](#)
12. A. Saunders, E. Z. Macosko, A. Wysoker, M. Goldman, F. M. Krienen, H. de Rivera, E. Bien, M. Baum, L. Bortolin, S. Wang, A. Goeva, J. Nemesh, N. Kamitaki, S. Brumbaugh, D. Kulp, S. A. McCarroll, Molecular diversity and specializations among the cells of the adult mouse brain. *Cell* **174**, 1015–1030.e16 (2018). [doi:10.1016/j.cell.2018.07.028](https://doi.org/10.1016/j.cell.2018.07.028) [Medline](#)

13. N. Rajakumar, K. Elisevich, B. A. Flumerfelt, Parvalbumin-containing GABAergic neurons in the basal ganglia output system of the rat. *J. Comp. Neurol.* **350**, 324–336 (1994). [doi:10.1002/cne.903500214](https://doi.org/10.1002/cne.903500214) [Medline](#)
14. A. Berndt, S. Y. Lee, J. Wietek, C. Ramakrishnan, E. E. Steinberg, A. J. Rashid, H. Kim, S. Park, A. Santoro, P. W. Frankland, S. M. Iyer, S. Pak, S. Ährlund-Richter, S. L. Delp, R. C. Malenka, S. A. Josselyn, M. Carlén, P. Hegemann, K. Deisseroth, Structural foundations of optogenetics: Determinants of channelrhodopsin ion selectivity. *Proc. Natl. Acad. Sci. U.S.A.* **113**, 822–829 (2016). [doi:10.1073/pnas.1523341113](https://doi.org/10.1073/pnas.1523341113) [Medline](#)
15. T. K. Roseberry, A. M. Lee, A. L. Lalive, L. Wilbrecht, A. Bonci, A. C. Kreitzer, Cell-Type-Specific Control of Brainstem Locomotor Circuits by Basal Ganglia. *Cell* **164**, 526–537 (2016). [doi:10.1016/j.cell.2015.12.037](https://doi.org/10.1016/j.cell.2015.12.037) [Medline](#)
16. S. K. Ogawa, J. Y. Cohen, D. Hwang, N. Uchida, M. Watabe-Uchida, Organization of monosynaptic inputs to the serotonin and dopamine neuromodulatory systems. *Cell Rep.* **8**, 1105–1118 (2014). [doi:10.1016/j.celrep.2014.06.042](https://doi.org/10.1016/j.celrep.2014.06.042) [Medline](#)
17. B. Weissbourd, J. Ren, K. E. DeLoach, C. J. Guenthner, K. Miyamichi, L. Luo, Presynaptic partners of dorsal raphe serotonergic and GABAergic neurons. *Neuron* **83**, 645–662 (2014). [doi:10.1016/j.neuron.2014.06.024](https://doi.org/10.1016/j.neuron.2014.06.024) [Medline](#)
18. X. Yu, W. Li, Y. Ma, K. Tossell, J. J. Harris, E. C. Harding, W. Ba, G. Miracca, D. Wang, L. Li, J. Guo, M. Chen, Y. Li, R. Yustos, A. L. Vyssotski, D. Burdakov, Q. Yang, H. Dong, N. P. Franks, W. Wisden, GABA and glutamate neurons in the VTA regulate sleep and wakefulness. *Nat. Neurosci.* **22**, 106–119 (2019). [doi:10.1038/s41593-018-0288-9](https://doi.org/10.1038/s41593-018-0288-9) [Medline](#)
19. S. Chowdhury, T. Matsubara, T. Miyazaki, D. Ono, N. Fukatsu, M. Abe, K. Sakimura, Y. Sudo, A. Yamanaka, GABA neurons in the ventral tegmental area regulate non-rapid eye movement sleep in mice. *eLife* **8**, e44928 (2019). [doi:10.7554/eLife.44928](https://doi.org/10.7554/eLife.44928) [Medline](#)
20. G. Cui, S. B. Jun, X. Jin, M. D. Pham, S. S. Vogel, D. M. Lovinger, R. M. Costa, Concurrent activation of striatal direct and indirect pathways during action initiation. *Nature* **494**, 238–242 (2013). [doi:10.1038/nature11846](https://doi.org/10.1038/nature11846) [Medline](#)
21. D. Gerashchenko, C. A. Blanco-Centurion, J. D. Miller, P. J. Shiromani, Insomnia following hypocretin2-saporin lesions of the substantia nigra. *Neuroscience* **137**, 29–36 (2006). [doi:10.1016/j.neuroscience.2005.08.088](https://doi.org/10.1016/j.neuroscience.2005.08.088) [Medline](#)
22. M. H. Qiu, R. Vetrivelan, P. M. Fuller, J. Lu, Basal ganglia control of sleep-wake behavior and cortical activation. *Eur. J. Neurosci.* **31**, 499–507 (2010). [doi:10.1111/j.1460-9568.2009.07062.x](https://doi.org/10.1111/j.1460-9568.2009.07062.x) [Medline](#)
23. Y. Y. Lai, T. Shalita, T. Hajnik, J.-P. Wu, J.-S. Kuo, L.-G. Chia, J. M. Siegel, Neurotoxic N-methyl-D-aspartate lesion of the ventral midbrain and mesopontine junction alters sleep-wake organization. *Neuroscience* **90**, 469–483 (1999). [doi:10.1016/S0306-4522\(98\)00429-1](https://doi.org/10.1016/S0306-4522(98)00429-1) [Medline](#)
24. Y. Oishi, Q. Xu, L. Wang, B.-J. Zhang, K. Takahashi, Y. Takata, Y.-J. Luo, Y. Cherasse, S. N. Schiffmann, A. de Kerchove d'Exaerde, Y. Urade, W.-M. Qu, Z.-

- L. Huang, M. Lazarus, Slow-wave sleep is controlled by a subset of nucleus accumbens core neurons in mice. *Nat. Commun.* **8**, 734 (2017). [doi:10.1038/s41467-017-00781-4](https://doi.org/10.1038/s41467-017-00781-4) [Medline](#)
25. X. S. Yuan, L. Wang, H. Dong, W.-M. Qu, S.-R. Yang, Y. Cherasse, M. Lazarus, S. N. Schiffmann, A. K. d'Exaerde, R.-X. Li, Z.-L. Huang, Striatal adenosine A<sub>2A</sub> receptor neurons control active-period sleep via parvalbumin neurons in external globus pallidus. *eLife* **6**, e29055 (2017). [doi:10.7554/eLife.29055](https://doi.org/10.7554/eLife.29055) [Medline](#)
26. J. C. Holstege, H. G. Kuypers, Brainstem projections to spinal motoneurons: An update. *Neuroscience* **23**, 809–821 (1987). [doi:10.1016/0306-4522\(87\)90160-6](https://doi.org/10.1016/0306-4522(87)90160-6) [Medline](#)
27. A. M. Lee, J. L. Hoy, A. Bonci, L. Wilbrecht, M. P. Stryker, C. M. Niell, Identification of a brainstem circuit regulating visual cortical state in parallel with locomotion. *Neuron* **83**, 455–466 (2014). [doi:10.1016/j.neuron.2014.06.031](https://doi.org/10.1016/j.neuron.2014.06.031) [Medline](#)
28. V. Caggiano, R. Leiras, H. Goñi-Erro, D. Masini, C. Bellardita, J. Bouvier, V. Caldeira, G. Fisone, O. Kiehn, Midbrain circuits that set locomotor speed and gait selection. *Nature* **553**, 455–460 (2018). [doi:10.1038/nature25448](https://doi.org/10.1038/nature25448) [Medline](#)
29. D. Kroeger, L. L. Ferrari, G. Petit, C. E. Mahoney, P. M. Fuller, E. Arrigoni, T. E. Scammell, Cholinergic, glutamatergic, and GABAergic neurons of the pedunculopontine tegmental nucleus have distinct effects on sleep/wake behavior in mice. *J. Neurosci.* **37**, 1352–1366 (2017). [doi:10.1523/JNEUROSCI.1405-16.2016](https://doi.org/10.1523/JNEUROSCI.1405-16.2016) [Medline](#)
30. D. J. Galtieri, C. M. Estep, D. L. Wokosin, S. Traynelis, D. J. Surmeier, Pedunculopontine glutamatergic neurons control spike patterning in substantia nigra dopaminergic neurons. *eLife* **6**, e30352 (2017). [doi:10.7554/eLife.30352](https://doi.org/10.7554/eLife.30352) [Medline](#)
31. W. W. Hauswirth, A. S. Lewin, S. Zolotukhin, N. Muzyczka, Production and purification of recombinant adeno-associated virus. *Methods Enzymol.* **316**, 743–761 (2000). [doi:10.1016/S0076-6879\(00\)16760-6](https://doi.org/10.1016/S0076-6879(00)16760-6) [Medline](#)
32. F. Osakada, E. M. Callaway, Design and generation of recombinant rabies virus vectors. *Nat. Protoc.* **8**, 1583–1601 (2013). [doi:10.1038/nprot.2013.094](https://doi.org/10.1038/nprot.2013.094) [Medline](#)
33. K. Miyamichi, Y. Shlomai-Fuchs, M. Shu, B. C. Weissbourd, L. Luo, A. Mizrahi, Dissecting local circuits: Parvalbumin interneurons underlie broad feedback control of olfactory bulb output. *Neuron* **80**, 1232–1245 (2013). [doi:10.1016/j.neuron.2013.08.027](https://doi.org/10.1016/j.neuron.2013.08.027) [Medline](#)
34. O. Ronneberger, P. Fischer, T. Brox, U-Net: Convolutional networks for biomedical image segmentation. *Lect. Notes Comput. Sci.* **9351**, 234–241 (2015). [doi:10.1007/978-3-319-24574-4\\_28](https://doi.org/10.1007/978-3-319-24574-4_28)
35. C. Xiao, W. Li, H. Deng, X. Chen, Y. Yang, Q. Xie, H. Han, Effective automated pipeline for 3D reconstruction of synapses based on deep learning. *BMC Bioinformatics* **19**, 263 (2018). [doi:10.1186/s12859-018-2232-0](https://doi.org/10.1186/s12859-018-2232-0) [Medline](#)

36. X. H. Gao, Memberships of the open cluster NGC 6405 based on a combined method: Gaussian mixture model and random forest. *Astron. J.* **156**, 121–133 (2018). [doi:10.3847/1538-3881/aad690](https://doi.org/10.3847/1538-3881/aad690)
37. P. Anikeeva, A. S. Andelman, I. Witten, M. Warden, I. Goshen, L. Grosenick, L. A. Gunaydin, L. M. Frank, K. Deisseroth, Optetrode: A multichannel readout for optogenetic control in freely moving mice. *Nat. Neurosci.* **15**, 163–170 (2011). [doi:10.1038/nn.2992](https://doi.org/10.1038/nn.2992) [Medline](#)
38. S. Zhang, M. Xu, W.-C. Chang, C. Ma, J. P. Hoang Do, D. Jeong, T. Lei, J. L. Fan, Y. Dan, Organization of long-range inputs and outputs of frontal cortex for top-down control. *Nat. Neurosci.* **19**, 1733–1742 (2016). [doi:10.1038/nn.4417](https://doi.org/10.1038/nn.4417) [Medline](#)
39. J. H. Song, Y.-H. Song, J.-H. Kim, W. Choi, S.-H. Lee, S.-B. Paik, Automated 3-D mapping of single neurons in the standard brain atlas using single brain slices. bioRxiv 373134 [Preprint] 20 July 2018 <https://doi.org/10.1101/373134>.